

# Temperature profiles of accretion disks in luminous active galactic nuclei derived from ultraviolet spectroscopic variability

Suyeon Son<sup>1,2</sup>, Minjin Kim<sup>1</sup>, and Luis C. Ho<sup>2,3</sup>

<sup>1</sup> Department of Astronomy and Atmospheric Sciences, Kyungpook National University, Daegu 41566, Korea  
e-mail: mkim.astro@gmail.com

<sup>2</sup> Kavli Institute for Astronomy and Astrophysics, Peking University, Beijing 100871, China

<sup>3</sup> Department of Astronomy, School of Physics, Peking University, Beijing 100871, China

Received

## ABSTRACT

The characteristic timescale ( $\tau$ ) of continuum variability of the accretion disk in active galactic nuclei (AGNs) is known to be related to the thermal timescale, which is predicted to scale with AGN luminosity ( $L$ ) and restframe wavelength ( $\lambda_{\text{RF}}$ ) as  $t_{\text{th}} \propto L^{0.5} \lambda_{\text{RF}}^2$  in the standard disk model. Using multi-epoch spectroscopic data from the Sloan Digital Sky Survey Reverberation Mapping project, we construct ultraviolet ensemble structure functions of luminous AGNs as a function of their luminosity and wavelength. Assuming that AGNs exhibit a single universal structure function when  $\Delta t$  is normalized by  $\tau$ , wherein  $\tau \propto L^a \lambda_{\text{RF}}^b$ , we find  $a = 0.50 \pm 0.03$  and  $b = 1.42 \pm 0.09$ . While the value of  $a$  aligns with the prediction from the standard disk model,  $b$  is significantly smaller than expected, suggesting that the radial temperature (color) profile of the accretion disk is significantly steeper (shallower) than the standard disk model. Notably, this discrepancy with theory has been observed in previous studies based on spectroscopic reverberation mapping and gravitational microlensing. Although no current model of accretion disks fully matches our results, our findings provide valuable constraints for testing future physical models.

**Key words.** galaxies: active — quasars: general

## 1. Introduction

While supermassive black holes (BHs) are ubiquitous in massive galaxies, only a minority of them are accreting sufficiently to shine as active galactic nuclei (AGNs). AGNs emit strong radiation over a wide range of wavelengths from the radio to the X-rays. In general, the emission from AGNs exhibits substantial variability with a timescale of days to years across all energies. In addition, variability originating from different substructures is found to be correlated (Matthews & Sandage 1963; Wagner & Witzel 1995; Ulrich et al. 1997). Under the assumption that the intrinsic variation in the accretion disk is echoed by extended structures such as the broad-line region (BLR) and the dusty torus with a time delay corresponding to the light crossing time, the radial size of such structures can be estimated by measuring time lags. Reverberation mapping (RM; Bahcall et al. 1972; Blandford & McKee 1982), first applied to probe the size of the BLR using the time delay between the variation in the accretion disk continuum and the broad emission lines (e.g., Peterson et al. 1994; O’Brien et al. 1998), subsequently led to the development of methods for estimating the masses of BHs in AGNs (e.g., Gebhardt et al. 2000; Peterson et al. 2004; Greene & Ho 2005; Vestergaard & Peterson 2006; Ho & Kim 2015; Wang & Woo 2024).

The RM method also provides a powerful probe of the size of the accretion disk (Krolik et al. 1991; Wanders et al. 1997). Simplifying the structure of an accretion disk into a series of annuli with a negative temperature gradient (i.e., lower temperature at larger radii), the time lag between the accretion disk continuum at different wavelengths, originating from different temperatures, can serve as a proxy for the disk

size. Intriguingly, disk sizes estimated from continuum RM are systematically larger (e.g., Fausnaugh et al. 2016; but see Homayouni et al. 2019) than predicted from the standard disk model (Shakura & Sunyaev 1973; Frank et al. 2002). A similar trend has also been identified through gravitational microlensing studies (e.g., Morgan et al. 2010). Various explanations have surfaced to explain this “disk size problem,” most based on a modification of the geometry or emitting source: accretion disk blown up by a disk wind (Sun et al. 2019), rimmed or rippled accretion disk (Starkey et al. 2023), X-ray source with enhanced height (Kammoun et al. 2019), disk reprocessing in the X-rays or far-ultraviolet (Gardner & Done 2017), or a significant contribution from the recombination continuum of the BLR (e.g., McHardy et al. 2018).

The radial profile of the effective temperature, defined as  $T \propto R^{-1/p}$ , can be used to test the validity of accretion disk models, as different models predict different temperature profiles. From an observational point of view, under the assumption that the radiation follows a blackbody spectrum ( $\lambda_{\text{max}} \propto T^{-1}$ ), it is more common to measure the more observationally tractable radial color profile,  $R \propto \lambda_{\text{RF}}^p$ , where  $\lambda_{\text{RF}}$  is the rest-frame wavelength. For example, while  $p = 4/3$  is expected from the standard disk model, a larger value of  $p$  is anticipated from the disk wind model (Li et al. 2019; Sun et al. 2019), while the opposite holds for the magneto-rotational instability model (Agol & Krolik 2000). Continuum RM studies find that the observed time lags for various wavelengths are well fit with  $p \approx 4/3$  as expected from the standard disk model (McHardy et al. 2014; Homayouni et al. 2019). However, both steeper ( $p < 4/3$ ; Fausnaugh et al. 2016; Starkey et al. 2017) and shallower ( $p > 4/3$ ; Jiang et al. 2017) profiles have been detected. The results

from microlensing studies are more controversial, reporting a wide range of values for  $p$ . While many claim that  $p$  is consistent with  $4/3$  (e.g., Eigenbrod et al. 2008; Poindexter et al. 2008; Rivera et al. 2023), values of  $p$  significantly less than  $4/3$  have been derived by Floyd et al. (2009), Blackburne et al. (2011), Jiménez-Vicente et al. (2014), and Muñoz et al. (2016). By contrast, Bate et al. (2018) and Cornachione & Morgan (2020) note an opposite trend. The origin of these discrepant results is unclear. Certainly, small-number statistics come into play, and it is difficult to judge the impact of sample selection and experimental methodology. It is vital to investigate the radial color profile for a large sample of AGNs using an independent method.

As a complementary approach, color profiles can be quantified using the characteristics of ultraviolet-optical variability arising from the accretion disk. This intrinsic variability can be characterized using the power spectral density, defined as the variability power as a function of frequency  $\nu$ . One can also compute the structure function (SF), defined as the variability amplitude as a function of time lag  $\Delta t$ . The power spectral density and SF of the accretion disk continuum are well fit with a broken power-law in the sense that the variability amplitude increases with increasing timescale and flattens above a certain characteristic timescale ( $\tau$ ; Kelly et al. 2009; MacLeod et al. 2010; Guo et al. 2017). Previous studies showed that  $\tau$  corresponds to the thermal timescale<sup>1</sup>  $t_{\text{th}}$  (Kelly et al. 2009; Sun et al. 2015; Burke et al. 2021; Arévalo et al. 2024; but see MacLeod et al. 2010). Although most studies reached a similar conclusion, their relations between  $\tau$  and AGN properties vary, possibly due to systematic uncertainties in the measurements of  $\tau$  caused by imperfect light curves with a sparse cadence and a relatively short baseline (Emmanoulopoulos et al. 2010; Kozłowski 2017).

Alternatively, the dependence of  $\tau$  on the AGN luminosity and wavelength can be investigated by assuming that all the SFs or power spectral densities follow a single universal function if  $\Delta t$  or  $\nu$  is converted to the units of the characteristic timescale. Applying this method to the broadband light curves of thousands of AGNs, Tang et al. (2023) demonstrated that  $\tau \propto L^{0.539 \pm 0.004} \lambda_{\text{RF, broad}}^{2.418 \pm 0.023}$ , where  $\lambda_{\text{RF}}$  is the effective wavelength of the broadband filter in the restframe. Although the slopes of the luminosity and wavelength factor are marginally steeper than expected from the standard disk model, this finding is broadly consistent with the predictions of the standard disk model on the thermal timescale (i.e.,  $\tau \propto L^{0.5} \lambda_{\text{RF}}^2$ ; but see Arévalo et al. 2024; Petrecca et al. 2024). Note that, in the standard disk model, the thermal timescale is expected to correlate with AGN luminosity and wavelength as  $\tau \propto L^{0.5} \lambda_{\text{RF}}^2$  (Shakura & Sunyaev 1973; Frank et al. 2002). This discrepancy is possibly due to several shortcomings of broadband photometry, including (1) contamination from broad emission lines and iron multiples (e.g., Boroson & Green 1992), (2) the broad range of the effective wavelength in the restframe depending on the redshift of the targets (e.g., MacLeod et al. 2010), and (3) time variation of the shape of the continuum (e.g., Guo & Gu 2016), which can introduce possible bias in converting broadband photometry to continuum flux. Despite these limitations, broadband monitoring data has been widely used, for they can be obtained efficiently for large samples compared to more resource-intensive spectroscopic monitoring, which is available only for more limited samples.

To properly investigate the dependence of  $\tau$  on the restframe wavelength, with the aim of constraining the temperature pro-

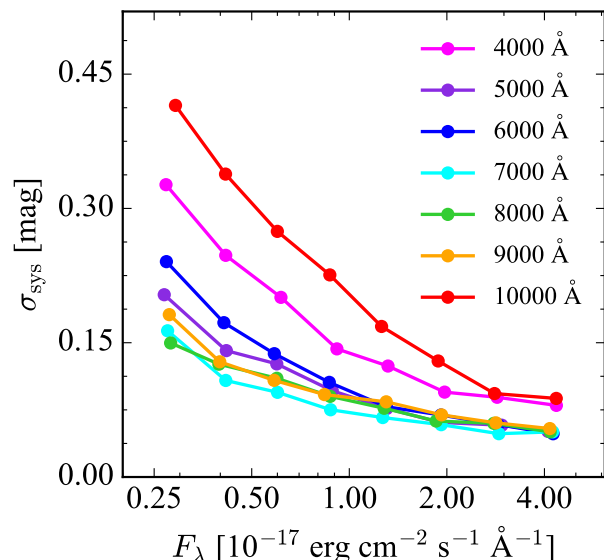


**Fig. 1.** Systematic uncertainty in magnitude due to uncertainty in flux calibration ( $\sigma_{\text{sys}}$ ) as a function of the observed wavelength and flux density. The systematic uncertainties increase dramatically at the blue and red ends of the spectra ( $\lambda_{\text{obs}} < 5000 \text{ \AA}$  and  $\lambda_{\text{obs}} > 9000 \text{ \AA}$ )

file of the accretion disk, it is preferable to measure the continuum variability using spectroscopic data, which can mitigate more effectively contaminants such as strong emission lines. The Sloan Digital Sky Survey Reverberation Mapping (SDSS-RM) project (Shen et al. 2015a, 2024), which has conducted intensive spectroscopic monitoring of a relatively large sample of quasars, provides an opportunity to carry out this experiment. With this dataset, we attempt to examine the dependence of the characteristic timescale of continuum variability on AGN luminosity and wavelength using spectroscopically determined continuum light curves.

## 2. Sample and data

The continuum variability of AGNs typically is studied using broadband photometry (e.g., Vanden Berk et al. 2004; MacLeod et al. 2010; Caplar et al. 2017; Tang et al. 2023; Arévalo et al. 2024). A shortcoming of this conventional method is that it can be contaminated easily by strong emissions from the BLR, including broad emission lines, the myriad blends from iron multiplets, and the Balmer continuum. By comparison, spectroscopic data offers the advantage that specific wavelength windows can be chosen to reject strong contaminants. This is the strategy we adopt in this study. We utilize the spectroscopic monitoring data from the SDSS-RM project<sup>2</sup> (Shen et al. 2015a, 2024) to construct the ultraviolet continuum SF. The SDSS-RM project monitored a flux-limited ( $i_{\text{PSF}} < 21.7 \text{ mag}$ ) sample of 849 quasars at  $0.1 < z < 4.5$  using a 2.5 m SDSS telescope with the BOSS spectrograph, covering the wavelength range  $3650 - 10400 \text{ \AA}$  at a spectral resolution of  $\sim 2000$ . Light curves from this project span  $\sim 7$  years with an average cadence of  $\sim 4, 12,$  and  $30$  days for the 2014, 2015–2017, and 2018–2020 observing seasons, respectively. Because accurate measurement of

<sup>1</sup> The thermal timescale is the approximate time it takes to establish thermal equilibrium.

<sup>2</sup> [https://ariel.astro.illinois.edu/sdssrm/final\\_result/](https://ariel.astro.illinois.edu/sdssrm/final_result/)

the continuum fluxes and their uncertainties is crucial to estimating the SF robustly, we compute those values directly from the spectra instead of extracting them from the best-fit continuum, which may lead to systematic bias.

### 2.1. Measurements of flux and its uncertainty

To measure the continuum variability using spectroscopic data, we define continuum windows at various wavelengths and estimate the flux densities from the single-epoch spectra within these regions. The uncertainties of the flux density are given in each spectral pixel for the single-epoch spectra. However, additional uncertainties stemming from imperfect flux calibration (e.g., Margala et al. 2016; Milaković et al. 2021) should be taken into account. We estimate the final uncertainty of the continuum flux ( $\sigma_{\text{final}}$ ) as the square root of the quadratic sum of these two sources of uncertainty.

The uncertainty measured from the continuum window with a width of  $40 \text{ \AA}$  is calculated as  $\sigma_{\text{flux}} / \sqrt{N}$ , where  $\sigma_{\text{flux}}$  is half the 16th to 84th percentile range of the flux density, and  $N$  is a number of data points within the continuum window. We use a median of the flux density within the continuum window as the flux at the continuum. For the systematic uncertainty due to the unstable flux calibration, we statistically estimated it using the multi-epoch spectra of our sample. If we assume that our sample does not vary within 2 days (i.e.,  $\text{SF}_{2\text{days}} \approx 0$ ), the observed flux variation within this time interval is caused solely by the systematics in the flux calibration. This systematic uncertainty, in units of magnitude, can be expressed as  $\sigma_{\text{sys}} = \sqrt{(\sigma_{\Delta\text{mag}} / \sqrt{2})^2 - \sigma_{\text{mag}}^2}$ , where  $\sigma_{\Delta\text{mag}}$  is half the 16th to 84th percentile range of the differences between magnitude pairs observed within 2 days<sup>3</sup>, and  $\sigma_{\text{mag}}$  is the uncertainty of the continuum flux in the single-epoch spectrum in units of magnitude (Figure 1). This value cannot be estimated for an individual object because the spectroscopic pairs observed within 2 days are typically fewer than seven for a single target, which is not sufficient to estimate the uncertainty. Instead, we derive the systematic uncertainties using the entire sample as a function of the observed wavelength ( $\lambda_{\text{obs}}$ ) and flux density ( $F_{\lambda}$ ). We find that it is sensitive to the observed wavelength and the brightness of the target (Figure 1). The systematic uncertainty of the single spectra at a specific wavelength is determined by interpolation.

Intriguingly,  $\sigma_{\text{sys}}$  is substantial at the spectral edges (e.g.,  $\lambda_{\text{obs}} < 5000 \text{ \AA}$  and  $\lambda_{\text{obs}} > 9000 \text{ \AA}$ ), indicating that the relative flux calibration error and imperfect sky subtraction may be severe in the original data. Motivated by this result, we opt not to use the spectral data at  $\lambda_{\text{obs}} < 5000 \text{ \AA}$  or  $\lambda_{\text{obs}} > 9000 \text{ \AA}$  in the observed frame. Additionally, we do not use objects with  $\sigma_{\text{final}} \geq 0.11 \text{ mag}$ , for which the noise dominates the variability because we cannot measure the error exactly for each object, but only statistically. Finally, to investigate the variability solely from the accretion disk, we attempt to avoid the spectral regions that can be highly contaminated by broad emission lines, the pseudo-continuum originating from Fe II multiplets (Shen et al. 2011), and the stellar continuum of the host galaxy. Consequently, the continuum fluxes are measured as median values within  $40 \text{ \AA}$ -wide continuum windows centered at 1367, 1479, 1746, 2230, 3050, 3500, and  $3800 \text{ \AA}$  in the rest frame. Note that the continuum fluxes at 3050 and  $3500 \text{ \AA}$  may be influenced by

<sup>3</sup> Note that the pair within 2 days is selected in the observed frame. Therefore, in the restframe,  $\Delta t$  between the pair is on average  $\sim 0.76 \pm 0.21$  days.

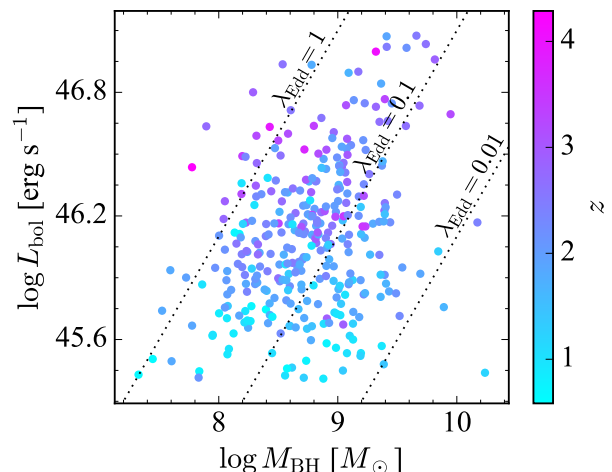


**Fig. 2.** Distribution of BH mass and bolometric luminosity of the final sample with available BH mass measurements. The points are color-coded by redshift. The dotted lines represent Eddington ratios of  $\lambda_{\text{Edd}} = 0.01, 0.1, \text{ and } 1$ .

the Balmer continuum (e.g., Cackett et al. 2018; Korista & Goad 2019). This phenomenon is further explored in Section 5.1. The width of the continuum window is set empirically to be wide enough to secure high signal-to-noise ratio fluxes ( $\text{S/N} \geq 3$ )<sup>4</sup> while at the same time minimizing the contribution from contaminants.

### 2.2. Sample selection

Before SF analysis, radio-loud sources ( $\sim 2\%$  of the initial sample), classified as those with flux density ratio between 6 cm and  $2500 \text{ \AA}$  (adopted from Shen et al. 2019) higher than 10 (Kellermann et al. 1989), are eliminated because of their distinctive variability characteristics (e.g., Wagner & Witzel 1995). We also discard light curves that lack any evidence of variability, based on the variability probability criterion  $P_{\text{var}} < 0.95$ , where  $P_{\text{var}}$ , calculated from  $\chi^2$  distribution (McLaughlin et al. 1996; Sánchez et al. 2017), is the probability that the target is intrinsically variable.  $P_{\text{var}}$  is computed for each continuum window using the  $\sim 7$  yr light curves and is commonly employed to confirm the intrinsic variability of the continuum flux through the  $\chi^2$  distribution. Note that S/N2, defined as  $\sqrt{\chi^2 - \text{DOF}}$ , where DOF is the number of degrees of freedom of the light curve, is used to quantify the variability of the emission flux (Grier et al. 2019). However, we choose not to use S/N2 in this study, as the criteria for the intrinsic variability are determined through visual inspection. To compute ensemble SF in Section 3, we divide the sample by bolometric luminosity, starting from  $\log(L_{\text{bol}}/\text{erg s}^{-1}) = 45.4$ , in steps of 0.25. Objects with luminosity lower than  $\log(L_{\text{bol}}/\text{erg s}^{-1}) \leq 45.4$  are removed because they can be substantially contaminated by the host galaxy ( $f_{\text{host}} \leq 0.1$  at  $3450 \text{ \AA}$ ; Shen et al. 2015b), even though we only use restframe ultraviolet wavelengths. The final sample consists of 447 AGNs that have light curves in at least one continuum window among 1367, 1479, 1746, 2230, 3050, 3500, and  $3800 \text{ \AA}$ . In total, 50, 85, 205, 322, 310, 249, and 197 light curves are available, respectively,

<sup>4</sup> More than 99% of the continuum measurements for the variable targets have an S/N of 3 or higher.

for the continuum windows at 1367, 1479, 1746, 2230, 3050, 3500, and 3800 Å.

### 2.3. AGN properties

To calculate the bolometric luminosity of the AGN, we adopt bolometric correction factors  $L_{\text{bol}} = 3.81 L_{1350\text{Å}}$  and  $L_{\text{bol}} = 5.15 L_{3000\text{Å}}$  (Richards et al. 2006; Shen et al. 2011). We use the median values of the monochromatic luminosities at 1350 Å and 3000 Å measured from 2014 to 2020 in the SDSS-RM project (Shen et al. 2024), giving priority to the former over the latter, as the bolometric correction factor for  $L_{3000\text{Å}}$  may not be constant and could vary with the AGN luminosity (e.g. Trakhtenbrot & Netzer 2012). BH masses are estimated from the RM method using H $\alpha$ , H $\beta$ , Mg II  $\lambda$ 2800, or C IV  $\lambda$ 1549. For those without successful measurements of time lags from RM, we adopt BH masses based on the single-epoch spectrum of H $\beta$  or C IV. We choose not to use BH mass estimates based on the single-epoch spectrum with Mg II because it appears to yield systematically lower values than that from Mg II RM. Our final sample of 447 quasars spans redshifts  $z = 0.58 - 4.29$ , AGN bolometric luminosities  $L_{\text{bol}} = 10^{45.4} - 10^{47.1}$  erg s $^{-1}$ , BH masses  $M_{\text{BH}} = 10^{7.3} - 10^{10.2} M_{\odot}$ , and Eddington ratios  $\lambda_{\text{Edd}} \equiv L_{\text{bol}}/L_{\text{Edd}} = 10^{-2.9} - 10^{0.6}$  (Figure 2), with Eddington luminosity  $L_{\text{Edd}} = 1.26 \times 10^{38} M_{\text{BH}}/M_{\odot}$  erg s $^{-1}$ .

### 3. Ensemble structure function

Following the definition from Press et al. (1992), the SF of an individual object is calculated as

$$\text{SF}^2(\Delta t) = \frac{1}{N_{\Delta t, \text{pair}}} \sum_{i=1}^{N_{\Delta t, \text{pair}}} (m(t) - m(t + \Delta t))^2 - \sigma_{\text{final}}^2(t) - \sigma_{\text{final}}^2(t + \Delta t), \quad (1)$$

where  $N_{\Delta t, \text{pair}}$  is the number of observed pairs with the time lag ( $\Delta t$ ),  $m$  is the observed magnitude, and  $\sigma_{\text{final}}$  is the final uncertainty of magnitude in the single-epoch spectrum, as described in Section 2.1. We adopt this SF definition because incomplete noise terms often lead to a flatter SF than the real SF (Kozłowski 2016). Because the SF can be highly sensitive to outliers, we apply  $3\sigma$  clipping to the median with half of the difference between 16th and 84th percentile of magnitude measurements in each light curve.

To examine the average SF as a function of luminosity and wavelength, we choose to use an ensemble SF instead of the SF from individual objects. The ensemble SF is calculated by averaging SF $^2$ s of sources in each luminosity and wavelength bin, considering that the SFs of individual sources are often associated with systematically large uncertainties and have negative values (e.g., Son et al. 2023; Kim et al. 2024). To avoid potential bias due to the small sample size, the ensemble SF is computed only if there are at least 10 objects in a group. Table 1 gives the number of objects used to estimate the ensemble SF and AGN properties for each group. The derived ensemble SFs in different luminosity and wavelength bins are shown in Figure 3.

To evaluate potential biases in estimating the ensemble SFs caused by the seasonal gaps and the limited baseline in the light curves, we perform the simulations using regularly sampled light curves with a cadence of one day, assuming the damped random walk model. Subsequently, we generate mock light curves, incorporating the actual cadence and redshift distributions of our sample. This experiment demonstrates that the ensemble SFs for

$\Delta t \lesssim 200$  days can be reproduced accurately using the simulated light curves (see also Emmanoulopoulos et al. 2010; Kozłowski 2017).

### 4. Results

To understand the physical origin of the variability, we examine how the characteristic timescale depends on the physical properties of AGNs. Previous studies demonstrated that  $\tau$  might correspond to the thermal timescale (Kelly et al. 2009, 2013; Caplar et al. 2017; Tang et al. 2023; Arévalo et al. 2024). In the standard disk model (Shakura & Sunyaev 1973; Frank et al. 2002), the thermal timescale correlates with the orbital timescale ( $t_{\text{orb}}$ ):

$$t_{\text{th}} \propto t_{\text{orb}} \alpha^{-1} \propto R_{\lambda}^{3/2} M_{\text{BH}}^{-1/2} \alpha^{-1}, \quad (2)$$

where  $R_{\lambda}$  is the characteristic disk radius responsible for continuum emission at the specific restframe wavelength, and  $\alpha$  is the viscosity parameter, assumed constant in the standard disk model. Since the disk radiates blackbody emission, its effective temperature ( $T$ ) at a given disk radius is given by

$$T(R) \propto (M_{\text{BH}} \dot{M} R^{-3})^{1/4}, \quad (3)$$

where  $\dot{M}$  is the mass accretion rate and  $R$  is the distance from the center of the disk. Using Wien's displacement law,  $\lambda_{\text{max}} \propto T^{-1}$ ,

$$R_{\lambda} \propto M_{\text{BH}}^{1/3} \dot{M}^{1/3} \lambda_{\text{RF}}^{4/3}. \quad (4)$$

From Equations (2) and (4) with an assumption of constant  $\alpha$  and  $L \propto \dot{M}$ , the thermal timescale is correlated with the luminosity and restframe wavelength ( $\lambda_{\text{RF}}^2$ ) as

$$t_{\text{th}} \propto L^{1/2} \lambda_{\text{RF}}^2. \quad (5)$$

To test whether this holds true for our dataset, we examine the dependence of  $\tau$  on the AGN luminosity and wavelength in the form

$$\tau \propto L_{\text{bol}}^a \lambda_{\text{RF}}^b. \quad (6)$$

The length of the light curves is insufficiently long to constrain  $\tau$  directly. Instead, we adopt an indirect method to investigate the dependence of  $\tau$  on the AGN luminosity and wavelength, assuming that all the SFs follow a single universal function if  $\Delta t$  is converted to units of  $\tau$  (e.g., Tang et al. 2023; Arévalo et al. 2024; Petrecca et al. 2024) as

$$\text{SF} = \delta(\Delta t/\tau)^{\gamma}, \quad (7)$$

where  $\gamma$  is the power-law slope of SF and  $\delta$  is the SF at  $\Delta t = \tau$ . Since  $\tau$  is derived in arbitrary units, the value of  $\delta$  also has no physical meaning in this study. Fitting the ensemble SFs of each luminosity group at different wavelengths, we can investigate the dependence of  $\tau$  on luminosity and wavelength. To achieve this, we first compute the ensemble SFs within luminosity bins for each continuum window and then fit them using the Python package `lmfit` to determine  $a$  and  $b$ .

We derive  $a = 0.50 \pm 0.03$  and  $b = 1.42 \pm 0.09$  (Figure 3b). Whereas the best-fit value of  $a$  is in excellent agreement with the predicted value of 0.5 from the standard disk model, the value of  $b$  is substantially smaller than the predicted value of 2, by more than  $6\sigma$  level. This reveals that the temperature (color) radial profile of the accretion disk deviates from the standard disk.

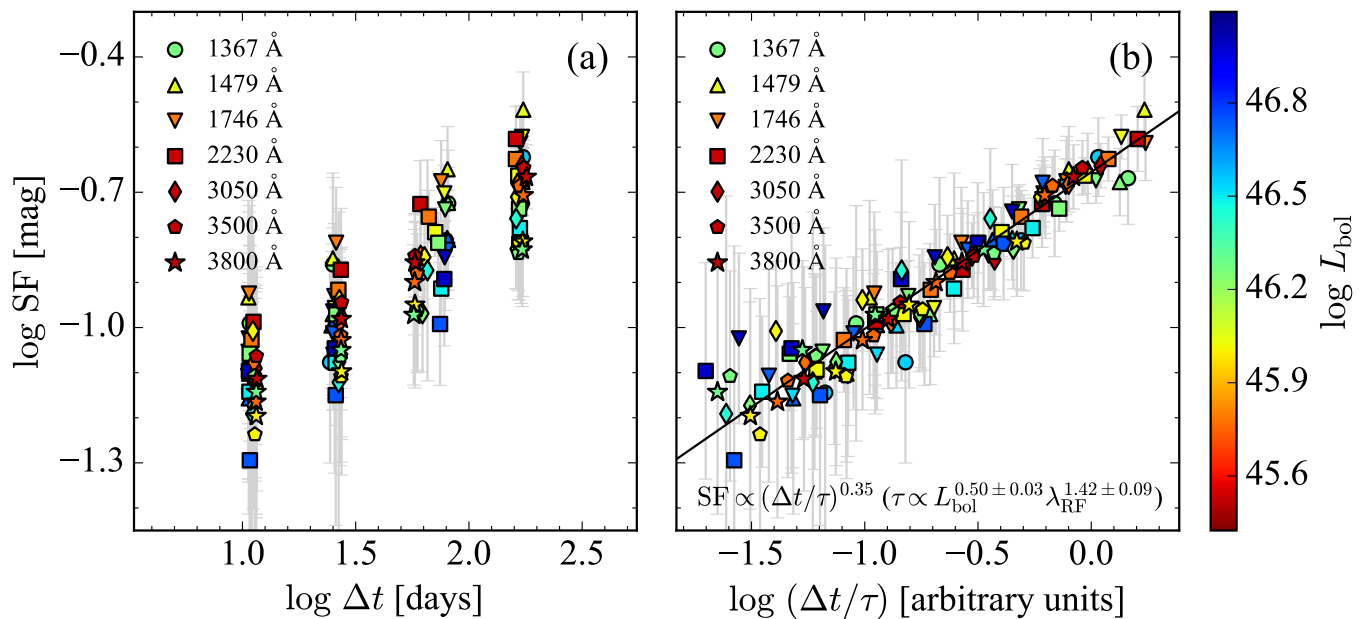


**Fig. 3.** Ensemble SF as a function of (a)  $\Delta t$  and (b)  $\Delta t/\tau$  at different wavelengths for each group color-coded by the average bolometric luminosity. Different symbols indicate different wavelengths used for continuum extraction. Panel (b) assumes that all the SFs follow a single universal function if  $\Delta t$  is converted to units of  $\tau \propto L_{\text{bol}}^a \lambda_{\text{RF}}^b$ . Note that values of  $\Delta t/\tau$  on the x-axis are only meaningful in relative terms. The solid black line represents the best-fit universal SF.

## 5. Discussion

### 5.1. Possible origins of distinctive color profile

The standard accretion disk is known to maintain its structure when the AGN is accreting at intermediate Eddington ratios of  $\lambda_{\text{Edd}} \approx 0.01 - 0.3$ . However, at least 100 objects in our final sample have  $\lambda_{\text{Edd}} \geq 0.3$ , and a handful of sources (four) have  $\lambda_{\text{Edd}} < 0.01$  (Fig. 2). Note that this is the minimum number because the Eddington ratio can only be calculated for the final sample with available BH mass measurements (i.e., BH mass based on the RM technique or broad C IV and H $\beta$  emissions from a single-epoch spectrum). When  $\lambda_{\text{Edd}} \geq 0.3$ , the cooling in the inner part of the disk is dominated by advection, which results in an optically and geometrically thick disk (“slim disk”: Begelman 1978; Abramowicz et al. 1988; Wang et al. 2014). At the opposite extreme end, when the accretion rates drop to low enough values and  $\lambda_{\text{Edd}} \lesssim 0.01$ , the accretion disk becomes optically thin and geometrically thick, transforming into a radiatively inefficient accretion flow (RIAF; Yuan & Narayan 2014; Ho 2008). The majority of central BHs in the local Universe reside in this state (Ho & Kim 2009; She et al. 2017). We test whether the distinctive color profile with  $\tau \propto \lambda_{\text{RF}}^{1.42}$  is due to the inclusion of objects having non-standard disks.

Here, we only focus on the impact of slim disks, as they account for nearly one-quarter of the final sample; highly sub-Eddington systems in the RIAF state account for less than 1% of our sources. Considering that a slim disk has a distinctive geometry, temperature profile, and kinematics compared to the standard disk, its characteristic timescale can differ from that of a standard disk (Beloborodov 1998; Wang & Zhou 1999; Watarai et al. 2000). However, the state change mostly occurs inside the photon-trapping radius of the slim disk, where the accretion disk becomes vertically extended due to the radiation pressure (Abramowicz et al. 1988; Wang & Zhou 1999; Sadowski 2011). To test if this phenomenon is directly related to our find-

ing, we first compute the photon-trapping radius and compare it with the effective emitting radius corresponding to the continuum wavelengths used in this study. The self-similar solution of Wang & Zhou (1999) for a slim disk expresses the photon-trapping radius as

$$R_{\text{tr}} = 0.9 \dot{m} R_g, \quad (8)$$

where  $\dot{m} = \dot{M}/\dot{M}_{\text{Edd}}$  is dimensionless accretion rate and  $R_g = 2GM/c^2$  is the Schwarzschild radius. In the same model, the effective temperature at a given radius  $R$  is given by

$$T_{\text{eff}} = 2.1 \times 10^7 (M_{\text{BH}}/M_{\odot})^{-1/4} (R/R_g)^{-1/2}. \quad (9)$$

Assuming that the slim disk radiates blackbody emission similar to a standard disk, using Wien’s displacement law ( $\lambda_{\text{max}} T = 2.898 \times 10^{-3} \text{ m K}$ ), the photon-trapping wavelength, where the radiation from the photon-trapping radius peaks, is calculated as (Wang & Zhou 1999; Cackett et al. 2020)

$$\lambda_{\text{tr}} = 1.3 (M_{\text{BH}}/M_{\odot})^{1/4} \dot{m}^{1/2} \text{ \AA}. \quad (10)$$

We note that  $\dot{m}$  cannot be directly measured for our sample because the BH spin and the viscous parameter are unknown. Therefore, we conservatively assume that the BH spin is 0 and the viscous parameter is 0.01, whereupon  $\dot{m}$  is highest and hence the photon-trapping radius is largest at a given Eddington ratio. With these assumptions, we estimate  $\dot{m}$  visually from Figure 4.11 of Sadowski (2011); the uncertainty of this visual estimate is  $\sim 3\%$  (0.01 dex). With the estimate of  $\dot{m}$  in hand, Equation (10) can then be used to deduce that the photon-trapping wavelength  $\lambda_{\text{tr}}$  for the majority of the sample ranges from  $\sim 300 \text{ \AA}$  to  $\sim 1350 \text{ \AA}$ , which is significantly shorter than the continuum

wavelengths (1367 – 3800 Å) used in this study<sup>5</sup>. The continuum fluxes analyzed here mostly originate from emitting regions outside the photon-trapping radius for highly accreting AGNs. It is also noteworthy that, from both theoretical (Watarai et al. 2000) and observational considerations (Li et al. 2024), the effective temperature profile of a slim disk outside of its photon-trapping radius is not markedly different from that of a standard thin disk. We conclude that the discrepancy of the  $\tau - \lambda_{\text{RF}}^b$  between this study ( $b = 1.43 \pm 0.09$ ) and the prediction from the standard disk ( $b = 2$ ) is unlikely to originate from the transition to the slim disk.

To test the impact of RIAFs, we additionally reject the four AGNs with RIAFs. The fit to Equation (6) remains almost the same ( $a = 0.49 \pm 0.03$ ,  $b = 1.43 \pm 0.09$ ). As a final sanity check, we apply the fit to the ensemble SFs for objects with  $0.01 < \lambda_{\text{Edd}} \leq 0.3$  that strictly speaking conform to the expectations of a standard disk, and still the results remain the same ( $a = 0.46 \pm 0.07$ ,  $b = 1.32 \pm 0.15$ ; Table 2). Neither slim disks nor RIAFs have a significant impact on our results.

Another factor that might contribute to the departure from the expected color profile is contamination from the Balmer pseudocontinuum originating from the BLR, which contributes  $\sim 10\%$  on average to the flux density at 3000 Å (Kovačević-Dojčinović et al. 2017). This pseudo-continuum has also been regarded as a culprit for the disk size problem identified from continuum RM studies (e.g., Fausnaugh et al. 2016; McHardy et al. 2018). To evaluate the possible effect of the Balmer continuum on our results, we refit Equation (6) by excluding wavelengths longer than 3000 Å, the spectral range most severely contaminated by the Balmer continuum (e.g., Cackett et al. 2018). The fitting results hardly change ( $a = 0.50 \pm 0.04$ ,  $b = 1.45 \pm 0.18$ ) within a  $1\sigma$  level. Therefore, the Balmer continuum does not seem to be the origin of the color profile discrepancy.

## 5.2. Comparison with observational studies

Various studies have investigated the color profiles in luminous AGNs based on light curves from broadband photometric data. For example, using the broadband data from the first year of the SDSS-RM project, Homayouni et al. (2019) found that the color profile ( $R \propto \lambda_{\text{RF}}^p$ ) is well fit with  $p = 1.28_{-0.39}^{+0.41}$ , equivalent to  $b = 3p/2 = 1.92_{-0.585}^{+0.615}$ . Their estimation is consistent with both the standard disk prediction and our best fit, considering their considerably larger uncertainties. Tang et al. (2023), employing the same method as ours, showed that the characteristic timescale is proportional to  $L^{0.539 \pm 0.004} \lambda^{2.418 \pm 0.023}$ ; their values of  $a$  and  $b$  are formally steeper than those predicted by the standard disk. It is unclear why their estimate of  $b$  is significantly larger than that of our study. We speculate that the discrepancy may arise from a potential bias introduced by the broadband photometry data. In addition, Tang et al. (2023) used a longer  $\Delta t$  (up to 350 days) compared to our study (up to 179 days). We impose this  $\Delta t$  limit because of the restricted baseline of our dataset (e.g., Emmanoulopoulos et al. 2010), which is more pronounced at shorter wavelengths (1367 and 1479 Å) because of cosmological time dilation. However, two studies based on photometric data offer counter-examples. Analyzing the characteristic timescales of thousands of individual quasars using  $\sim 10$

<sup>5</sup> The only exception is a single object for which  $\lambda_{\text{tr}} = 1482$  Å is larger than 1367 and 1479 Å. Omitting this target hardly changes the fit of Equation (6).

years of broadband light curves from the SDSS Stripe 82 region (Jiang et al. 2014), MacLeod et al. (2010) found  $\tau \propto \lambda_{\text{RF}}^{0.17 \pm 0.02}$ . Similarly, Stone et al. (2022) (see erratum in Stone et al. 2023) studied  $\sim 20$  years of broadband light curves for 190 SDSS Stripe 82 quasars and found  $\tau \propto \lambda_{\text{RF}}^{0.35 \pm 0.14}$  or  $\lambda_{\text{RF}}^{0.43 \pm 0.01}$  depending on the sample selection. These works produced significantly shallower slopes than our study. The situation for continuum RM based on spectroscopic data is no less confusing. While the work of Fausnaugh et al. (2016) and Starkey et al. (2017) yielded  $p = 0.99 \pm 0.14$  or  $b = 1.49 \pm 0.21$ , which agrees well with our best-fit results, most are at variance, with a preponderance of studies supporting  $p \approx 4/3$  (Cackett et al. 2018; Collier et al. 1998; Homayouni et al. 2019; Guo et al. 2022).

Microlensing analysis, too, has produced a wide diversity of power-law indices, ranging from  $p \approx 4/3$  (Eigenbrod et al. 2008; Poindexter et al. 2008; Rivera et al. 2023) to  $p < 4/3$  (Floyd et al. 2009; Blackburne et al. 2011; Jiménez-Vicente et al. 2014; Muñoz et al. 2016) and  $p > 4/3$  (Bate et al. 2018; Cornachione & Morgan 2020). It is noteworthy that microlensing studies based on spectroscopic data and/or narrowband photometric data have a tendency to favor smaller values of the power-law index ( $p \approx 0.7 - 1.3$  or  $b \approx 1.05 - 1.95$ ; Eigenbrod et al. 2008; Mediavilla et al. 2011; Mosquera et al. 2011; Motta et al. 2012; Jiménez-Vicente et al. 2014; Muñoz et al. 2016) compared to the prediction from the standard disk model, which qualitatively aligns with our study.

Overall, the above examples underscore that estimates of radial temperature profiles of accretion disks can be sensitive to the adopted methodology and sample selection. They also highlight the merits of using spectroscopic data, as adopted in this work, instead of the more expedient broadband photometry.

## 5.3. Application to accretion disk model

Assuming that AGNs obey a universal SF, we find that the characteristic timescale ( $\tau$ ) is proportional to  $L^{0.5}$  and  $\lambda_{\text{RF}}^{1.42}$ . While the luminosity dependence is consistent with the prediction from the standard disk theory, the wavelength scaling reveals that the radial temperature profile is considerably steeper than that of a standard disk. After careful consideration of factors that might affect the analysis, we conclude that this discrepancy in the temperature profile is likely to be genuine.

There is presently no obvious resolution to this dilemma. From a theoretical point of view, a steep temperature (and hence shallow color) profile can be partly explained by the magneto-rotational instability model attributed to additional dissipation originating from torque at the inner edge of the accretion disk. For example, the magneto-rotational instability model of Agol & Krolik (2000) predicts a power-law index of  $p = 8/7 = 1.14$  ( $b = 12/7 = 1.71$ ), which is marginally smaller than  $p = 4/3$  ( $b = 2$ ), although not as small as our observed value of  $b = 1.42$ . On the other hand, the plethora of scenarios that have been proposed to solve the disk size problem either do not focus on the temperature profile or they predict temperature profiles contradicting our results (e.g., Lawrence 2012; Gardner & Done 2017; Kammoun et al. 2019; Li et al. 2019; Sun et al. 2019, 2020; Starkey et al. 2023). For instance, Lawrence (2012) argued that reprocessed continuum emission, presumably due to cold, dense clouds located at  $\sim 30R_S$ , may be crucial to explain the disk size problem. Contrary to our results, however, a steeper temperature profile is expected from this model. In a similar manner, the disk wind model favors not only a steeper temperature profile but also a larger power-law index for the AGN luminosity (i.e.,  $a > 0.5$ ; Li et al. 2019;

Sun et al. 2019). The temperature profile of the rimmed accretion disk model of Starkey et al. (2023) does not depart substantially (i.e.,  $T \propto R^{-3/4}$ ) from that of the standard disk except for the outer part of the disk.

## 6. Conclusion

We construct ultraviolet ensemble SFs of luminous AGNs grouped by luminosity and continuum wavelength using spectrophotometric data obtained through the SDSS-RM project. Assuming that all AGNs share a single universal SF after  $\Delta t$  is normalized by the characteristic timescale ( $\tau$ ), we fit all the ensemble SFs to investigate how the characteristic timescale depends on luminosity and wavelength in the form  $\tau \propto L^a \lambda_{\text{RF}}^b$ . Our main findings are.

- The ensemble SFs are well fit by a single universal SF( $\Delta t/\tau$ ) with  $a = 0.50 \pm 0.03$  and  $b = 1.42 \pm 0.09$ .
- The dependence of  $\tau$  on luminosity ( $a = 0.50 \pm 0.03$ ) is in excellent agreement with the predicted value of  $a = 0.5$  from the standard disk model.
- The dependence of  $\tau$  on continuum wavelength ( $b = 1.42 \pm 0.09$ ) departs by more than  $6\sigma$  from the standard disk model ( $b = 2$ ), revealing a shallower color (steeper temperature) profile.
- Highly accreting AGNs and Balmer continuum have a negligible effect on measurements of  $b$ , strongly suggesting that the discrepancy between the observed and predicted value of  $b$  is genuine.
- Interestingly, our estimation of  $b$  based on spectroscopic variability is in broad agreement with previous continuum RM and microlensing analysis based on spectroscopic monitoring data. This suggests that spectroscopic data may yield more robust results on the radial temperature or color profiles than photometric data.

*Acknowledgements.* We are grateful to the anonymous referee for constructive comments and suggestions that greatly improved our manuscript. LCH was supported by the National Science Foundation of China (11991052, 12233001), the National Key R&D Program of China (2022YFF0503401), and the China Manned Space Project (CMS-CSST-2021-A04, CMS-CSST-2021-A06). This work was supported by the National Research Foundation of Korea (NRF) grant funded by the Korean government (MSIT) (Nos. 2022R1A4A3031306, 2023R1A2C1006261, and RS-2024-00347548).

## References

Abramowicz, M. A., Czerny, B., Lasota, J. P., & Szuszkiewicz, E. 1988, *ApJ*, 332, 646  
 Agol, E. & Krolik, J. H. 2000, *ApJ*, 528, 161  
 Arévalo, P., Churazov, E., Lira, P., et al. 2024, *A&A*, 684, A133  
 Bahcall, J. N., Kozlovsky, B.-Z., & Salpeter, E. E. 1972, *ApJ*, 171, 467  
 Bate, N. F., Vernardos, G., O'Dowd, M. J., et al. 2018, *MNRAS*, 479, 4796  
 Begelman, M. C. 1978, *MNRAS*, 184, 53  
 Beloborodov, A. M. 1998, *MNRAS*, 297, 739  
 Blackburne, J. A., Pooley, D., Rappaport, S., & Schechter, P. L. 2011, *ApJ*, 729, 34  
 Blandford, R. D. & McKee, C. F. 1982, *ApJ*, 255, 419  
 Boroson, T. A. & Green, R. F. 1992, *ApJS*, 80, 109  
 Burke, C. J., Shen, Y., Blaes, O., et al. 2021, *Science*, 373, 789  
 Cackett, E. M., Chiang, C.-Y., McHardy, I., et al. 2018, *ApJ*, 857, 53  
 Cackett, E. M., Gelbord, J., Li, Y.-R., et al. 2020, *ApJ*, 896, 1  
 Caplar, N., Lilly, S. J., & Trakhtenbrot, B. 2017, *ApJ*, 834, 111  
 Collier, S. J., Horne, K., Kaspi, S., et al. 1998, *ApJ*, 500, 162  
 Cornachione, M. A. & Morgan, C. W. 2020, *ApJ*, 895, 93  
 Eigenbrod, A., Courbin, F., Meylan, G., et al. 2008, *A&A*, 490, 933  
 Emmanoulopoulos, D., McHardy, I. M., & Uttley, P. 2010, *MNRAS*, 404, 931  
 Fausnaugh, M. M., Denney, K. D., Barth, A. J., et al. 2016, *ApJ*, 821, 56

Floyd, D. J. E., Bate, N. F., & Webster, R. L. 2009, *MNRAS*, 398, 233  
 Frank, J., King, A., & Raine, D. J. 2002, *Accretion Power in Astrophysics: Third Edition*  
 Gardner, E. & Done, C. 2017, *MNRAS*, 470, 3591  
 Gebhardt, K., Bender, R., Bower, G., et al. 2000, *ApJL*, 539, L13  
 Greene, J. E. & Ho, L. C. 2005, *ApJ*, 630, 122  
 Grier, C. J., Shen, Y., Horne, K., et al. 2019, *ApJ*, 887, 38  
 Guo, H., Barth, A. J., & Wang, S. 2022, *ApJ*, 940, 20  
 Guo, H. & Gu, M. 2016, *The Astrophysical Journal*, 822, 26  
 Guo, H., Wang, J., Cai, Z., & Sun, M. 2017, *ApJ*, 847, 132  
 Ho, L. C. 2008, *ARA&A*, 46, 475  
 Ho, L. C. & Kim, M. 2009, *ApJS*, 184, 398  
 Ho, L. C. & Kim, M. 2015, *ApJ*, 809, 123  
 Homayouni, Y., Trump, J. R., Grier, C. J., et al. 2019, *ApJ*, 880, 126  
 Jiang, L., Fan, X., Bian, F., et al. 2014, *ApJS*, 213, 12  
 Jiang, Y.-F., Green, P. J., Greene, J. E., et al. 2017, *ApJ*, 836, 186  
 Jiménez-Vicente, J., Mediavilla, E., Kochanek, C. S., et al. 2014, *ApJ*, 783, 47  
 Kammoun, E. S., Papadakis, I. E., & Dovčiak, M. 2019, *ApJL*, 879, L24  
 Kellermann, K. I., Sramek, R., Schmidt, M., Shaffer, D. B., & Green, R. 1989, *AJ*, 98, 1195  
 Kelly, B. C., Bechtold, J., & Siemiginowska, A. 2009, *ApJ*, 698, 895  
 Kelly, B. C., Treu, T., Malkan, M., Pancoast, A., & Woo, J.-H. 2013, *ApJ*, 779, 187  
 Kim, M., Son, S., & Ho, L. C. 2024, *A&A*, 689, A27  
 Korista, K. T. & Goad, M. R. 2019, *MNRAS*, 489, 5284  
 Kovačević-Dojčinović, J., Marčeta-Mandić, S., & Popović, L. Č. 2017, *Frontiers in Astronomy and Space Sciences*, 4, 7  
 Kozłowski, S. 2016, *ApJ*, 826, 118  
 Kozłowski, S. 2017, *A&A*, 597, A128  
 Krolik, J. H., Horne, K., Kallman, T. R., et al. 1991, *ApJ*, 371, 541  
 Lawrence, A. 2012, *MNRAS*, 423, 451  
 Li, R., Ho, L. C., Ricci, C., & Trakhtenbrot, B. 2024, *ApJ*, 975, 50  
 Li, Y.-P., Yuan, F., & Dai, X. 2019, *MNRAS*, 483, 2275  
 MacLeod, C. L., Ivezić, Z., Kochanek, C. S., et al. 2010, *ApJ*, 721, 1014  
 Margala, D., Kirkby, D., Dawson, K., et al. 2016, *ApJ*, 831, 157  
 Mathews, T. A. & Sandage, A. R. 1963, *ApJ*, 138, 30  
 McHardy, I. M., Cameron, D. T., Dwelley, T., et al. 2014, *MNRAS*, 444, 1469  
 McHardy, I. M., Connolly, S. D., Horne, K., et al. 2018, *MNRAS*, 480, 2881  
 McLaughlin, M. A., Mattox, J. R., Cordes, J. M., & Thompson, D. J. 1996, *ApJ*, 473, 763  
 Mediavilla, E., Muñoz, J. A., Kochanek, C. S., et al. 2011, *ApJ*, 730, 16  
 Milaković, D., Webb, J. K., Lee, C.-C., & Zavyagin, E. O. 2021, *A&A*, 655, A53  
 Morgan, C. W., Kochanek, C. S., Morgan, N. D., & Falco, E. E. 2010, *ApJ*, 712, 1129  
 Mosquera, A. M., Muñoz, J. A., Mediavilla, E., & Kochanek, C. S. 2011, *ApJ*, 728, 145  
 Motta, V., Mediavilla, E., Falco, E., & Muñoz, J. A. 2012, *ApJ*, 755, 82  
 Muñoz, J. A., Vives-Arias, H., Mosquera, A. M., et al. 2016, *ApJ*, 817, 155  
 O'Brien, P. T., Dietrich, M., Leighly, K., et al. 1998, *ApJ*, 509, 163  
 Peterson, B. M., Berlind, P., Bertram, R., et al. 1994, *ApJ*, 425, 622  
 Peterson, B. M., Ferrarese, L., Gilbert, K. M., et al. 2004, *ApJ*, 613, 682  
 Petrecca, V., Papadakis, I. E., Paolillo, M., De Cicco, D., & Bauer, F. E. 2024, *A&A*, 686, A286  
 Poindexter, S., Morgan, N., & Kochanek, C. S. 2008, *ApJ*, 673, 34  
 Press, W. H., Rybicki, G. B., & Hewitt, J. N. 1992, *ApJ*, 385, 404  
 Richards, G. T., Lacy, M., Storrie-Lombardi, L. J., et al. 2006, *ApJS*, 166, 470  
 Rivera, A. B., Morgan, C. W., Florence, S. M., et al. 2023, *ApJ*, 952, 54  
 Sadowski, A. 2011, arXiv e-prints, arXiv:1108.0396  
 Sánchez, P., Lira, P., Cartier, R., et al. 2017, *ApJ*, 849, 110  
 Shakura, N. I. & Sunyaev, R. A. 1973, *A&A*, 24, 337  
 She, R., Ho, L. C., & Feng, H. 2017, *ApJ*, 842, 131  
 Shen, Y., Brandt, W. N., Dawson, K. S., et al. 2015a, *ApJS*, 216, 4  
 Shen, Y., Greene, J. E., Ho, L. C., et al. 2015b, *ApJ*, 805, 96  
 Shen, Y., Grier, C. J., Horne, K., et al. 2024, *ApJS*, 272, 26  
 Shen, Y., Hall, P. B., Horne, K., et al. 2019, *ApJS*, 241, 34  
 Shen, Y., Richards, G. T., Strauss, M. A., et al. 2011, *ApJS*, 194, 45  
 Son, S., Kim, M., & Ho, L. C. 2023, *ApJ*, 958, 135  
 Starkey, D., Horne, K., Fausnaugh, M. M., et al. 2017, *ApJ*, 835, 65  
 Starkey, D. A., Huang, J., Horne, K., & Lin, D. N. C. 2023, *MNRAS*, 519, 2754  
 Stone, Z., Shen, Y., Burke, C. J., et al. 2022, *MNRAS*, 514, 164  
 Stone, Z., Shen, Y., Burke, C. J., et al. 2023, *MNRAS*, 521, 836  
 Sun, M., Trump, J. R., Shen, Y., et al. 2015, *ApJ*, 811, 42  
 Sun, M., Xue, Y., Brandt, W. N., et al. 2020, *ApJ*, 891, 178  
 Sun, M., Xue, Y., Trump, J. R., & Gu, W.-M. 2019, *MNRAS*, 482, 2788  
 Tang, J.-J., Wolf, C., & Tonry, J. 2023, *Nature Astronomy*, 7, 473  
 Trakhtenbrot, B. & Netzer, H. 2012, *MNRAS*, 427, 3081  
 Ulrich, M.-H., Maraschi, L., & Urry, C. M. 1997, *ARA&A*, 35, 445  
 Vanden Berk, D. E., Willite, B. C., Kron, R. G., et al. 2004, *ApJ*, 601, 692  
 Vestergaard, M. & Peterson, B. M. 2006, *ApJ*, 641, 689  
 Wagner, S. J. & Witzel, A. 1995, *ARA&A*, 33, 163  
 Wanders, I., Peterson, B. M., Alloin, D., et al. 1997, *ApJS*, 113, 69  
 Wang, J.-M., Qiu, J., Du, P., & Ho, L. C. 2014, *ApJ*, 797, 65  
 Wang, J.-M. & Zhou, Y.-Y. 1999, *ApJ*, 516, 420  
 Wang, S. & Woo, J.-H. 2024, *ApJS*, 275, 13  
 Watarai, K.-y., Fukue, J., Takeuchi, M., & Mineshige, S. 2000, *PASJ*, 52, 133  
 Yuan, F. & Narayan, R. 2014, *ARA&A*, 52, 529

**Table 1.** Properties for the Subsamples

Wavelength (1)	$G$ (2)	$N$ (3)	$z$ (4)	$\log(L_{\text{bol}}/\text{erg s}^{-1})$ (5)	$\log(M_{\text{BH}}/M_{\odot})$ (6)	$\log \lambda_{\text{Edd}}$ (7)
1367	3	15(15)	2.91	46.27	8.67	-0.50
	4	15(15)	3.22	46.54	8.61	-0.17
1479	2	17(17)	2.63	46.04	8.66	-0.72
	3	26(26)	2.77	46.25	8.77	-0.62
	4	19(19)	2.98	46.54	8.79	-0.35
	5	10(10)	2.83	46.72	9.19	-0.58
1746	1	28(28)	2.09	45.80	8.63	-0.93
	2	55(55)	2.30	46.03	8.63	-0.70
	3	60(60)	2.42	46.25	8.82	-0.67
	4	31(31)	2.59	46.52	8.87	-0.44
	5	13(13)	2.68	46.73	9.21	-0.59
	6	10(9)	2.58	46.99	9.40	-0.50
2230	0	24(6)	1.44	45.53	8.34	-0.94
	1	79(53)	1.69	45.79	8.68	-0.98
	2	82(65)	1.89	46.02	8.68	-0.76
	3	74(59)	2.04	46.25	8.88	-0.73
	4	30(28)	2.21	46.49	8.95	-0.55
	5	15(12)	2.20	46.74	9.15	-0.50
3050	0	62(28)	1.17	45.52	8.62	-1.20
	1	74(43)	1.39	45.77	8.67	-1.01
	2	52(30)	1.51	46.02	8.74	-0.82
	3	35(18)	1.47	46.25	8.78	-0.64
	4	10(7)	1.63	46.45	9.01	-0.66
	3500	0	48(23)	1.09	45.53	8.60
1		50(27)	1.24	45.76	8.59	-0.94
2		25(11)	1.26	46.00	8.78	-0.86
3		19(8)	1.28	46.27	8.63	-0.48
3800	0	34(21)	1.02	45.53	8.52	-1.09
	1	32(21)	1.10	45.76	8.60	-0.94
	2	15(8)	1.12	46.00	8.66	-0.73
	3	11(7)	1.14	46.29	8.53	-0.36

**Notes.** Col. (1): Central wavelength of continuum windows in the rest frame. Col. (2): Group divided by bolometric luminosity; 0 =  $45.4 < \log(L_{\text{bol}}/\text{erg s}^{-1}) \leq 45.65$ , 1 =  $45.65 < \log(L_{\text{bol}}/\text{erg s}^{-1}) \leq 45.9$ , 2 =  $45.9 < \log(L_{\text{bol}}/\text{erg s}^{-1}) \leq 46.15$ , 3 =  $46.15 < \log(L_{\text{bol}}/\text{erg s}^{-1}) \leq 46.4$ , 4 =  $46.4 < \log(L_{\text{bol}}/\text{erg s}^{-1}) \leq 46.65$ , 5 =  $46.65 < \log(L_{\text{bol}}/\text{erg s}^{-1}) \leq 46.9$ , and 6 =  $46.9 < \log(L_{\text{bol}}/\text{erg s}^{-1}) \leq 47.15$ . Col. (3): Number of objects; in parentheses is the number of objects with BH mass estimates. Col. (4): Average redshift. Col. (5): Average bolometric luminosity. Col. (6): Average BH mass. Col. (7): Average Eddington ratio.

**Table 2.** Best-fit parameters for  $\tau \propto L^a \lambda_{\text{RF}}^b$ 

Subsample (1)	$a$ (2)	$b$ (3)
All	$0.50 \pm 0.03$	$1.42 \pm 0.09$
$0.01 < \lambda_{\text{Edd}} \leq 0.3$	$0.46 \pm 0.07$	$1.32 \pm 0.15$
All with $\lambda_{\text{RF}} < 3000 \text{ \AA}$	$0.50 \pm 0.04$	$1.45 \pm 0.18$